Quantitative Hydroxyl Radical Footprinting Reveals Cooperative Interactions between DNA-Binding Subdomains of PU.1 and IRF4†

Petra Gross,‡ Adelinda A. Yee,§ Cheryl H. Arrowsmith,§ and Robert B. Macgregor, Jr.*,‡

Department of Pharmaceutical Sciences, and Department of Medical Biophysics, University of Toronto and Ontario Cancer Institute, Toronto, Ontario, Canada

Received December 23, 1997; Revised Manuscript Received May 6, 1998

ABSTRACT: Quantitative hydroxyl radical footprinting and fluorescence polarization measurements have been used to determine the dissociation constants (K_d) of complexes between the *ets* domain of the murine transcription factor PU.1 and three different DNA fragments. Two natural PU.1 binding sites, the SV40 enhancer site and the λB motif of $Ig_{\lambda 2-4}$ enhancer, were used as well as the PU.1 binding site present in the crystallized PU.1−DNA complex. With the use of quantitative hydroxyl radical footprinting we obtained binding isotherms for individual protected nucleotides and contact sites on both strands of the DNA. K_d values of $(1.53 \pm 0.12) \times 10^{-8}$ M were found for the λB element, $(3.60 \pm 0.65) \times 10^{-8}$ M for the SV40 enhancer site, and $(2.28 \pm 0.27) \times 10^{-8}$ M for the sequence used in the crystal structure. In addition, the binding of a second protein, the DNA binding domain of IRF4, to the λB site by itself and in the presence of PU.1 was analyzed. The IRF4 DBD shows three footprints on the TTCC strand and one footprint on the GGAA strand of the λB element. The dissociation constant for the binary IRF4 DBD−λB complex equals $(5.59 \pm 0.60) \times 10^{-7}$ M. The K_d value of the IRF4−λB interaction is reduced by a factor of 5 in the presence of two different DNA-bound PU.1 protein constructs, PU.1 DBD and a PU.1 construct containing the PEST domain (PU.1-PEST). A similar decrease of the K_d value was observed for the binding of PU.1-PEST in the presence of DNA-bound IRF4 DBD demonstrating a cooperative interaction between the PU.1-PEST and IRF4 DBD. On the basis of the hydroxyl radical footprints in the ternary PU.1/IRF4/λB complex, a model for the interactions between the two proteins and the λB site was developed. The DNA binding domains of both proteins bind the DNA in the major groove with potential protein−protein interactions near the intervening minor groove.

The transcription factor PU.1 is a member of the *ets* gene family (*1*). The *ets* proteins share a conserved 85-amino acid DNA binding domain, the *ets* domain, that recognizes the core DNA sequence 5′-GGAA-3′ (*1*, *2*). The three-dimensional structure of the *ets* domain of PU.1 in a complex with a 16-bp[1] DNA fragment has been resolved by X-ray crystallography (*3*). In the crystal the DNA is bent toward the protein by 8° and curved almost uniformly along the DNA fragment. The DNA binding motif of PU.1 has been described as a winged loop-helix-loop architecture (*3*).

PU.1 is involved in the expression of numerous genes that regulate the maturation of B-cells and the differentiation of mast cells and macrophages (*1*). The immunoglobulin (Ig) light-chain gene enhancers $E_{k3'}$ and $E_{\lambda 2-4}$ contain a conserved DNA element essential to their activities (*4*). These DNA sites are bound by PU.1 and a second nuclear factor (*4*), IRF4 (*5*). IRF4 is also referred to as Pip (PU.1 interacting protein) (*4*), LSRIF (*6*), NF-EM5 (*7*), and ICSCAT (*8*). IRF4 belongs to a growing family of transcription factors called interferon regulatory factors (IRF) (for review, see ref *9*). IRF4 is closely related to the interferon consensus sequence binding protein (ICSBP) and, like ICBSP, IRF4 is expressed specifically in lymphoid tissues in both B- and T-cell lines (*4*, *6*).

IRF4 and PU.1 bind adjacent sites on the Ig light-chain enhancer sequence (*10*, *11*). Whereas PU.1 binds the DNA within the enhancer element by itself, the binding of the full-length IRF4 protein to DNA depends on the presence of DNA-bound PU.1 (*4*, *7*). Furthermore, the formation of the ternary complex requires phosphorylation of S148, an amino acid within the PEST domain (Pro-, Glu-, Ser-, Thr-rich domain) of PU.1 (*12*). A hypothetical model of the PU.1/IRF4/DNA complex formation has been proposed (*13*). Upon interaction of IRF4 with the PU.1 region around S148, the DNA binding domain of IRF4 contacts the DNA. In

† This work was supported in part by a research scholarship from the Deutsche Forschungsgemeinschaft to P.G., and grants from the Natural Science and Engineering Research Council of Canada (to R.B.M.) and the Medical Research Council of Canada (to C.H.A.). C.H.A. is an MRC Scholar.

* Author to whom correspondence should be addressed at Department of Pharmaceutical Sciences, University of Toronto, 19 Russell Street, Toronto, Ontario, M5S 2S2, Canada. Phone: (416) 978-7332. Fax: (416) 978-8511. E-mail: macgreg@phm.utoronto.ca.

‡ Department of Pharmaceutical Sciences, University of Toronto, Toronto, Ontario, M5S 2S2.

§ Department of Medical Biophysics, University of Toronto and Ontario Cancer Institute, Toronto, Ontario, M5G 2M9.

[1] Abbreviations: bp, base pair; IRF, interferon regulatory factors; ISRE, interferon-stimulated response element; Ig, immunoglobulin; DBD, DNA binding domain; BSA, bovine serum albumin; dNTP, deoxyribonucleotide triphosphate; PCR, polymerase chain reaction; DTT, dithiothreitol; PMSF, phenylmethylsulfonyl fluoride; PEST, proline-, glutamine-, serine-, threonine-rich domain.

S0006-2960(97)03144-9 CCC: $15.00
Published on Web 06/12/1998

addition, protein−protein interactions between the DNA binding domains of PU.1 and IRF4 in the ternary complex were proposed (*13*).

Hydroxyl radical footprinting is a useful method to elucidate specific interactions within protein−DNA complexes on a single base level. The footprints accurately reflect the solvent environment around the DNA in a complex (*14*). The thermodynamics of DNA binding by one or more proteins is accessible by quantitative footprinting. The free energy of binding has been obtained for several protein−DNA systems (for a recent review, see ref *15*). Whereas most quantitative footprinting studies have used DNase I as a cleaving agent, only a few investigations have employed hydroxyl radical footprinting to obtain more detailed thermodynamical and structural information about protein−DNA complexes (*16*−*19*).

In this article, we present isotherms obtained by quantitative hydroxyl radical footprinting for the binding of the *ets* domain of murine PU.1 to different DNA fragments. We also present data on the interaction of the DNA binding domain of human IRF4 to the λB element on a single base level. The λB DNA composite contains a PU.1 binding site and, downstream from the core recognition sequence GGAA, a binding site for IRF4. The interactions of IRF4 with the DNA are monitored in the absence of PU.1 and in the presence of two different PU.1 constructs, one containing the *ets* domain of murine PU.1, and the other containing the *ets* domain plus the PEST domain of murine PU.1. Cooperative interactions between the DNA binding domains of IRF4 and both PU.1 constructs were determined and quantified.

MATERIALS AND METHODS

Enzymes and Chemicals. BSA and T4 polynucleotide kinase were purchased from New England Biolabs Inc., *Taq* DNA polymerase came from Gibco BRL. The dNTP's and poly(dI-dC)·poly(dI-dC) were obtained from Pharmacia Biotech. Ammonium iron(II) sulfate hexahydrate and L-ascorbic acid (sodium salt) were from Aldrich, EDTA (disodium salt) and 30% aqueous hydrogen peroxide came from Fisher Biotech. [γ-^{32}P]ATP was purchased from Amersham Corp.

DNA Preparation. The cloning of the three different plasmids used in this study, pCRYSK, pPUSK, and pLBSK, and the amplification of the 100-bp DNA fragments using PCR have been previously described (*20*). pCRYSK contains the 16-bp sequence that was used for the crystallography of the *ets* domain of PU.1 (*3*), pPUSK contains a 17-bp region of the SV40 enhancer (*7*), and pLBSK contains the central 23-bp region of the λB site of the murine $Ig_{\lambda 2-4}$ enhancer (*7*, *11*). The DNA concentration was estimated from the intensity of the ethidium bromide-stained band of a control PCR reaction.

Proteins. Different C-terminal PU.1 constructs and the N-terminal DNA binding domain (DBD) of IRF4 were overexpressed and purified according to published protocols (*21*). The DBD of IRF4 contains amino acids 20−137 of human IRF4 protein, which are identical to murine IRF4 in this region of the protein. The DBD of PU.1 consists of amino acids 161−272 of murine PU.1, the longer PU.1 construct includes the PEST domain and contains amino acids 106−272. Except for the longer PU.1 construct, the $(His)_6$ tag which facilitates the purification process was cleaved off the protein constructs (*20*). The purity of the protein samples was verified by polyacrylamide gel electrophoresis. The bands were visualized by Coomassie Blue staining. The DBD of PU.1 and IRF4 were stored in a buffer containing 25 mM sodium phosphate, pH 6.5, and 0.1 mM PMSF. The longer PU.1 construct was dialyzed at 4 °C against a buffer containing 10 mM Tris HCl, pH 7.6, 50 mM NaCl, 1 mM EDTA, 1 mM DTT, and 0.1 mM PMSF. The protein concentrations were estimated from the absorbance at 280 nm based on molar extinction coefficients calculated using the GCG software package (Genetics Computer Group, Inc): 22190 M^{-1} cm^{-1} for the PU.1 DBD, 24810 M^{-1} cm^{-1} for PU.1 (106−272), and 33690 M^{-1} cm^{-1} for the IRF4 DBD. All protein samples were stored at −20 °C in aliquots until needed.

Hydroxyl Radical Footprinting. The procedure used in the present experiments was carried out as previously described (*20*), with the following minor modifications. Aliquots of known protein concentration were serially diluted up to 10000-fold. From each diluted solution 1, 2, 5, or 7 μL were transferred to a reaction vial containing 2 μL of a 10× binding buffer and 1 μL of end-labeled DNA at ∼0.75 nM (20000−30000 cpm). The total volume of the binding solution was adjusted to 17 μL by addition of sterile water, and the reaction was allowed to equilibrate at 22 °C for 1 h. The final concentrations of buffer were 10 mM Tris-HCl, pH 7.6, 50 mM NaCl, 1 mM EDTA, 1 μg BSA, 1 μg poly(dI-dC)·poly(dI-dC). In the experiments in which two proteins are studied, the first protein was added at saturating concentrations (0.1 μM PU.1 DBD, 0.3 μM PU.1-PEST, and 7 μM IRF4 DBD) and allowed to equilibrate in the binding solution with the end-labeled DNA for at least 1 h prior to the addition of the titrant protein. Then, a second 1-h incubation step followed.

After equilibration, the footprinting reaction was carried out by adding 3 μL of a cleavage solution containing 133 μM ammonium iron(II) sulfate hexahydrate solution, 266 μM EDTA, 6.7 mM sodium ascorbate, and 0.33% hydrogen peroxide. The cleavage reaction was allowed to proceed for 2 min at 22 °C. It was terminated by adding 4 μL of a solution containing 50 mM thiourea and 0.1 M EDTA, and then kept on ice until all samples were cleaved. The reaction solutions were lyophilized and subsequently dissolved in loading buffer containing 90% formamide and heat denatured at 95 °C for 4 min. The DNA samples were resolved by electrophoresis on an 8% polyacrylamide denaturing gel (7 M urea). The gels were dried and the band pattern was visualized using an Ambis model 4000 radioanalytic imaging system.

Numerical Data Analysis. The device we used to visualize the gel patterns directly detects β-particles by their ability to ionize gas atoms. Typically, an exposure time of 16 h was sufficient to clearly visualize all bands of interest. Further analysis and quantification was performed with ONE-dscan software (Scanalytics Inc., Billerica, MA). The density profiles for each lane consist of a series of peaks and valleys corresponding to maxima and minima of the ^{32}P intensity and hence the location of bands and interband spaces on the gel image. The peak intensities were obtained by integrating a Gaussian fit to each peak. The accuracy of the calculated

Gaussian profile and the original density profile was verified for each lane. To allow a comparison of integrated band densities from different lanes, the lanes were normalized to eliminate pipetting and loading errors. In each lane the integrated band densities of at least six bands well outside the footprinting region were summed. The integrated density of each peak was then multiplied by a normalization factor equal to the quotient of the integrated normalizing peaks of the control lane (lane without any protein) over the sum of the integrated normalizing peaks in the respective lane being analyzed. Then, the normalized, integrated band densities were converted to fractional protection (p) according to eq 1,

$$p = 1 - \frac{I_N(n)}{I_{N,0}(n)} \quad (1)$$

where I_N (n) is the normalized integrated density of nucleotide n in the presence of protein and $I_{N,0}$ (n) is the normalized integrated density of the same nucleotide from a lane without any protein. Fractional saturation (Y) of individual nucleotides and binding sites was determined from the fractional protection data (*22*−*24*). The binding data were fit simultaneously for the binding constant and the upper and lower transition endpoints according to eq 2 using SigmaPlot 4.0 software (SPSS Inc., Chicago, IL)

$$f = m\mathrm{Y} + b \quad (2)$$

where

$$Y = \frac{K_B[\mathrm{P}]}{1 + K_B[\mathrm{P}]} \quad (3)$$

and $m = {}^{1}/_{(\mathrm{UL}-\mathrm{LL})}$, and $b = {}^{\mathrm{LL}}/_{(\mathrm{LL}-\mathrm{UL})}$ where LL and UL are the lower and the upper titration endpoints. K_B is the equilibrium binding constant, and [P] is the concentration of free protein. The dissociation constant (K_d) equals the reciprocal value of K_B. Since the DNA concentration used was much lower than the resulting K_d, [P] is very close to the total protein concentration. The binding curves presented in the figures were scaled to Y using the best-fit transition endpoints.

Fluorescence Anisotropy Measurements. The DNA fragments used in the fluorescence experiments were fluorescein-labeled at the 3′ end of the GGAA strand. The DNA oligonucleotides given below were purchased from Dalton Chemical Laboratories (Toronto, ON), and the respective fluorescein-labeled strands were annealed with their complementary DNA strands.

CRYSK	5' AAA AAG GGG AAG TGG G 3'-Fluorescein
	3' TTT TTC CCC TTC ACC C 5'
PUSK	5' CTG AAA GAG GAA CTT TGG TA 3'-Fluorescein
	3' GAC TTT CTC CTT GAA ACC AT 5'
LBSK	5' ATA AAA GGA AGT GAA ACC AAG 3'-Fluorescein
	3' TAT TTT CCT TCA CTT TGG TTC 5'

The concentration of double-stranded DNA was determined from the absorbance at 260 nm assuming that an optical density equal to 1 at 260 nm was equivalent to 0.15 mM nucleotides. Protein concentrations were estimated as described above. The binding buffer used in these experiments contained 25 mM sodium phosphate adjusted to pH 6.5. A volume of 700 μL of PU.1 DBD (30 μM) was equilibrated with 1 nM fluorescein-labeled DNA at 22 °C, and the fluorescence polarization was measured using a Beacon2000 Analyzer (Pan Vera Corp., Madison, WI) in accordance with the manufacturer's recommendations (Beacon Application Guide, 1995). Then 100 μL of binding buffer containing fluorescein-labeled DNA (1 nM) was added, and the fluorescence polarization was determined again. This addition of binding buffer with fluorescein-labeled DNA was repeated until the polarization readings approached those of the binding buffer containing only the fluorescein-labeled DNA. The resulting polarization data were converted to anisotropy as described by Lundblad et al. (*25*). Dissociation constants were determined by fitting the anisotropy data to eq 2 as described for the footprinting data. The anisotropy value of the free DNA was used as the lower endpoint of the binding curve.

RESULTS

Figure 1 shows the different DNA fragments used for footprinting. The binding sites of PU.1, marked with arrowheads, are almost identical among the different target sequences (*20*).

Binding Isotherms for the Interaction of the PU.1-DBD to Different DNA Sequences. Each of the three double-stranded DNA sequences was titrated with the *ets* domain of PU.1. Figure 2 shows a representative titration footprinting gel using λB DNA labeled on the TTCC strand. Binding curves were calculated for each nucleotide within the S1 protection site of the complex and representative binding isotherms for T(10), A(12), and C(13) are shown in Figure 3A. Less protected nucleotides (for example, position 14) and the weaker footprint (S2 in Figure 2) had a lower signal-to-noise ratio and were not quantified.

In addition to the binding isotherms for single nucleotides, a titration curve for the entire S1 footprinting region was determined. The normalized band densities of nucleotides 10−14 were summed and further processed as described for single nucleotides. The binding isotherm obtained for the footprinting region in the PU.1−λB complex is shown in Figure 3B. In comparison to Figure 3A, it shows improvement in the signal arising from summation of several peak intensities. The dissociation constants (K_d) calculated from the binding isotherms of the λB site are summarized in Table 1 (column 3). The antisense strand of the λB DNA was also used to quantify the interactions of the longer PU.1-PEST construct, amino acids 106−272, and the resulting K_d values are given in column 4 of Table 1. Table 1 also contains the K_d values obtained from the binding isotherms for individual nucleotides and the entire footprinting region of the pCRYSK and pPUSK fragments (columns 1 and 2).

The interactions of PU.1 with the GGAA strands of the three DNA fragments were also monitored. Figure 4A shows the result of titration of PU.1 with the sequence used in the crystal structure (pCRYSK) labeled on the GGAA strand.

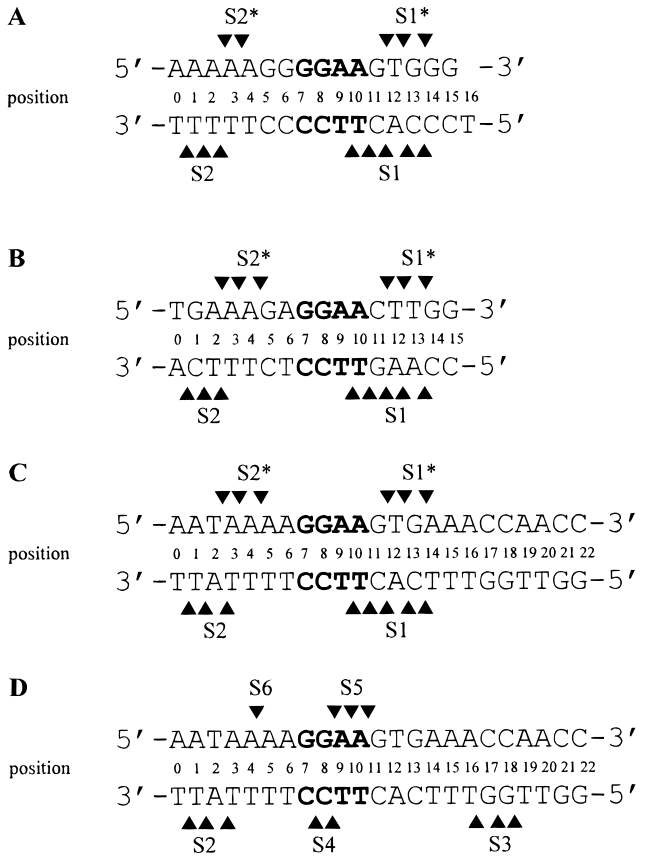

FIGURE 1: Comparison of the interactions between the *ets* domain of PU.1 and different target sequences. The consensus sequence is shown in bold, and the backbone positions protected from hydroxyl radical cleavage are indicated with solid arrowheads (*20*). The nucleotide 5′ to each arrowhead is missing in the gel pattern and discussed in the text as a protected nucleotide. Groups of contiguous protected nucleotides are labeled as protection sites S1−S6. (A) The sequence of the PU.1 binding region of the DNA fragment pCRYSK contains the sequence used for crystallography of the PU.1−DNA complex (*3*). (B) DNA sequence and footprints obtained for the pPUSK−PU.1 complex (*20*). The sequence shown here is identical to the SV40 enhancer site (*7*). (C) DNA sequence and footprints for the pLBSK−PU.1 complex (*20*). The sequence aligned here corresponds to the λB site of the $Ig_{\lambda 2-4}$ enhancer (*11*). (D) DNA sequence and footprints for the λB−IRF4 DBD complex. The protected sites are marked as described in the text.

As previously reported (*20*), the protection of the GGAA strand by the binding of PU.1 results in a less pronounced footprint compared to the TTCC strand. Nevertheless, we determined the binding isotherms for most nucleotides within the two protection sites S1* and S2* (marked in Figure 4A). The resulting binding curves for A(2), T(12), and G(13) are displayed in Figure 4B. Table 2 contains the K_d values obtained for the interaction of PU.1 DBD with the GGAA strand of pCRYSK together with the data for the sense strands of pLBSK and pPUSK calculated from corresponding footprinting gels (gels not shown).

Fluorescence Anisotropy Measurements. The binding of PU.1 to DNA was also measured with fluorescence anisotropy. Figure 5 shows the dependence of the fluorescence anisotropy of the three different fluorescein-labeled sequences on the concentration of the PU.1 DBD. The dissociation constants from the binding curves are given in the bottom row of Table 2. The K_d values are 1 order of magnitude higher than those determined in the footprinting experiments (Tables 1 and 2).

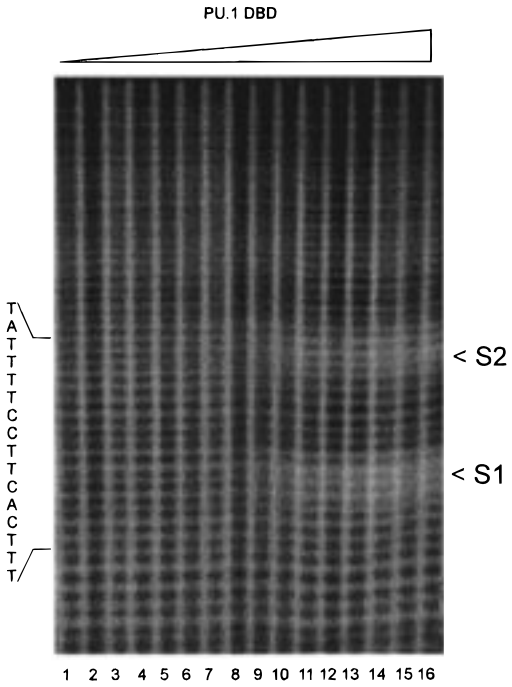

FIGURE 2: Titration of the TTCC strand of the pLBSK fragment with PU.1 DBD monitored with hydroxyl radical footprinting. 30000 cpm of ^{32}P-end-labeled DNA at ∼0.75 nM were used in each lane. Lane 1 contains no protein; in lanes 2 to 16, increasing amounts of PU.1 DBD are used. The two protected sites of PU.1 are marked with S1 and S2, respectively.

Interaction of IRF4 with DNA. The DNA binding domain of human IRF4 (amino acid residues 20−137) was investigated with regard to its ability to bind the λB site. Figure 6A shows the densitometric traces obtained for the TTCC strand of the λB DNA in the presence of the IRF4 DBD. Three protected sites are evident, T(1)A(2)T(3) marked as S2, C(8)T(9), two nucleotides within the recognition sequence (marked as S4), and a region of three nucleotides further upstream from the TTCC core sequence, G(17)G(18)T(19) (indicated as S3, see also Figure 1D). Interestingly, while PU.1 does not show any close contacts with the phosphates of the GGAA recognition sequence in the PU.1−DNA complex (Figure 1C), the DNA binding domain of IRF4 does contact phosphates within the PU.1 core recognition sequence. A second interesting characteristic of the IRF4−DNA interactions is that S2, T(1)A(2)T(3), is also protected by PU.1 (Figure 1, panels C and D). The protection pattern for the GGAA strand of the λB DNA sequence is shown in Figure 6B. The IRF4 construct protects the DNA at G(8)A(9)A(10) within the recognition sequence, marked as S5, and at position A(4), marked as S6 (Figure 1D). The IRF4 interactions with S4, C(8)T(9), and S3, G(17)G(18)T(19), on the TTCC strand of the λB DNA fragment were quantified from corresponding titration footprinting gels. The protection at the S2 site on the TTCC strand and at the S5 and S6 sites on the GGAA strand were not intense enough to yield satisfactory binding curves. Figure 7B shows binding isotherms for the S3 and S4 sites (closed symbols), and column 1 of Table 3 summarizes the dissociation constants for these sites as well as the K_d values derived from binding curves of the individual nucleotides within S3.

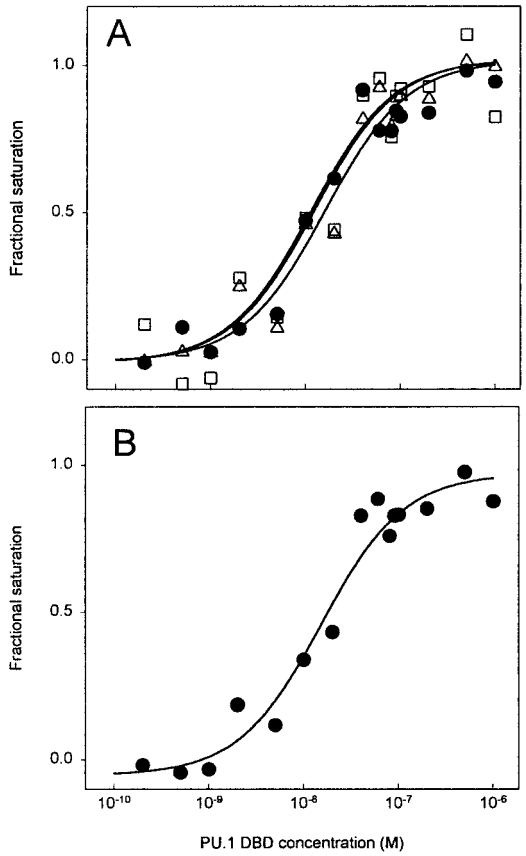

FIGURE 3: Binding isotherms for the interaction of PU.1 DBD with the TTCC strand of pLBSK. (A) Protection curves of single nucleotides, (●) T(10), (△) A(12), and (□) C(13) were determined as described in Material and Methods. The solid lines represent the fitted binding curves using eq 2. (B) The binding curve for the entire binding site shown in Figure 1C. The solid line is the fitted binding isotherm.

Table 1: Dissociation Constants, K_d ($\times 10^{-8}$ M), for the Interactions of PU.1 DBD and PU.1 (106−272) with the TTCC Strands of the Different DNA Fragments

						pLBSK	
nucleotide[a]		pCRYSK		pPUSK		PU.1 DBD	PU.1 (106−272)
10	T	2.42 ± 0.77[b]	T	2.76 ± 0.38	T	1.15 ± 0.10	6.69 ± 2.07
11	C	3.36 ± 1.04	G	4.14 ± 1.36	C	2.01 ± 0.18	4.55 ± 0.96
12	A	2.52 ± 0.38	A	4.39 ± 1.18	A	1.61 ± 0.16	4.66 ± 1.03
13	C	2.66 ± 0.64	A	3.77 ± 1.02	C	1.24 ± 0.14	4.77 ± 1.48
10−14[c]		2.28 ±0.27		3.60 ± 0.65		1.53 ± 0.12	5.83 ± 1.28
+ IRF4 DBD[d]						1.08 ± 0.11	1.22 ± 0.66

[a] Numeration system for the nucleotides is shown in Figure 1. [b] Mean ± standard error. [c] Corresponds to the entire binding site including the nucleotides 10−14, the K_d was determined as described in Results. [d] The K_d values for the entire binding site (nucleotides 10−14) in the presence of DNA-bound IRF4 DBD.

Interactions of IRF4 and PU.1 with the λB Site. These experiments were designed to elucidate the interactions in the ternary complex of PU.1 and IRF4 with the λB site. The first set of experiments investigated the interactions of the IRF4 DBD construct with the λB element, labeled on the TTCC strand, in the presence of the *ets* domain of PU.1. Figure 7A shows the result of a titration of the IRF4 DBD in the presence of a saturating constant concentration of PU.1 DBD. The DNA was incubated with PU.1 DBD at a final concentration of 0.1 μM prior to the addition of IRF4 to

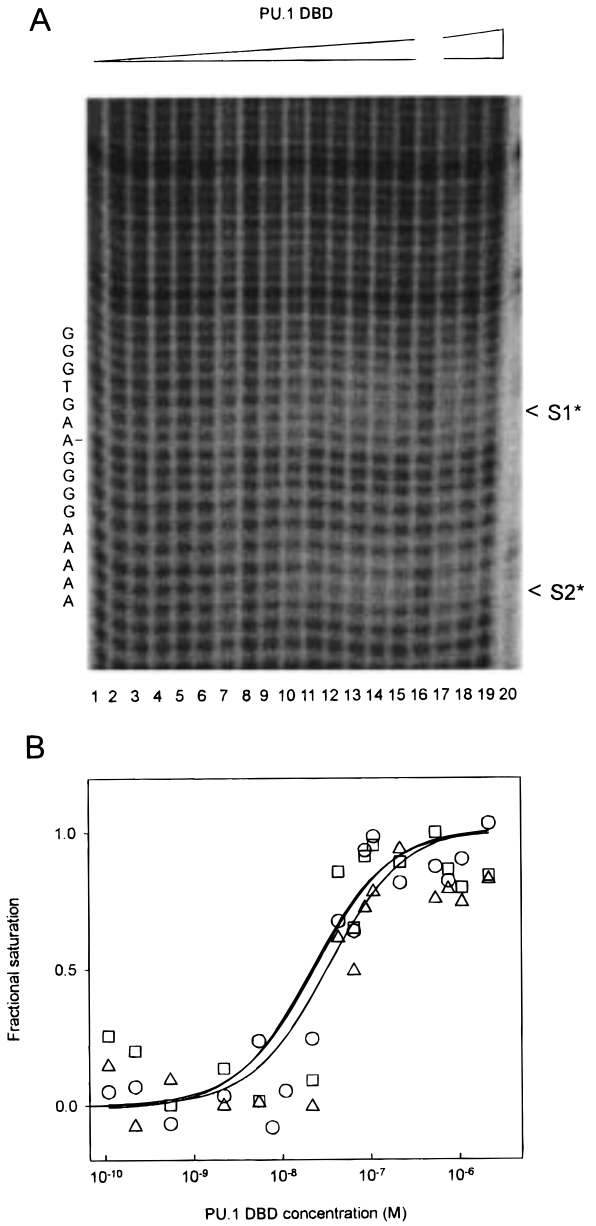

FIGURE 4: (A) Titration of the GGAA strand of the pCRYSK fragment with PU.1 DBD followed with hydroxyl radical footprinting. 30000 cpm of ^{32}P-end-labeled DNA at ∼0.75 nM were used in each lane. In lanes 1−15 and 17−19, increasing amounts of PU.1 DBD are used. Lane 16 shows the cutting pattern in the absence of PU.1, and lane 20 contains the uncleaved DNA fragment. The two protection sites of PU.1 DBD are marked with S1* and S2*, respectively. (B) The protection curves for (○) A(2), (△) T(12), and (□) G(13) were determined from the gel shown in Figure 4A. The binding data were fit with the use of eq 2 (solid lines).

ensure an equilibrated PU.1−DNA complex. The two contact sites in the PU.1−DNA complex are clearly visible (labeled S1 and S2), a third footprint arises in lane 9 due to the interaction of IRF4 with the nucleotides G(17)G(18)T-(19) (marked with S3). Two additional bands, C(8)T(9), become partially protected from hydroxyl radical cleavage with increasing IRF4 concentration (S4). The binding of IRF4 at T(1)A(2)T(3) is not visible in this gel since this DNA region is already protected by PU.1 (S2). The dissociation constants for the two footprint regions S3 and S4, and those derived from the binding curves of individual nucleotides within S3, were determined from the gel in Figure 7A and

Table 2: Dissociation Constants, K_d ($\times 10^{-8}$ M) for the Interactions of PU.1 DBD with the GGAA Strands of the Target DNA Sequences

nucleotide[a]		pCRYSK		pPUSK		pLBSK
2	A	3.33 ± 0.70[b]	A	1.15 ± 0.14	T	nd
3	A	2.33 ± 0.54	A	1.94 ± 0.36	A	2.40 ± 0.31
4	A	np[c]	A	nd	A	2.78 ± 0.30
2−4		3.28 ± 0.71		1.28 ± 0.14		3.33 ± 0.66
11	G	nd[d]	C	nd	G	nd
12	T	2.38 ± 0.40	T	2.25 ± 0.38	T	2.26± 0.72
13	G	2.17 ± 0.45	T	1.39 ± 0.18	G	1.48± 0.28
11−13		2.14 ± 0.26		1.40 ± 0.20		2.00 ± 0.31
fluorescence[e]		66.8 ± 11.6		18.9 ± 2.3		69.2 ± 8.7

[a] Numeration system of nucleotides is given in Figure 1. [b] Mean ± standard error. [c] Not protected. [d] Not determined. [e] K_d were determined using fluorescence polarization as described in Materials and Methods.

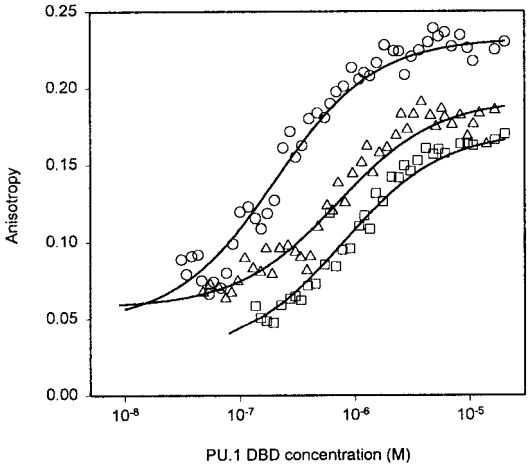

FIGURE 5: Binding of PU.1 DBD to different target sequences determined by fluorescence anisotropy. Three different oligonucleotides were used: (○) PUSK, 20-bp DNA sequence identical to SV 40 enhancer site (Figure 1B); (△) CRYSK, 16-bp sequence used in the crystal structure (shown in Figure 1A), and (□) LBSK, 21-bp sequence containing the λB site DNA (Figure 1C). The anisotropy of the free DNA was taken as the lower endpoint of each binding curve. The data were normalized and fitted as described in Materials and Methods.

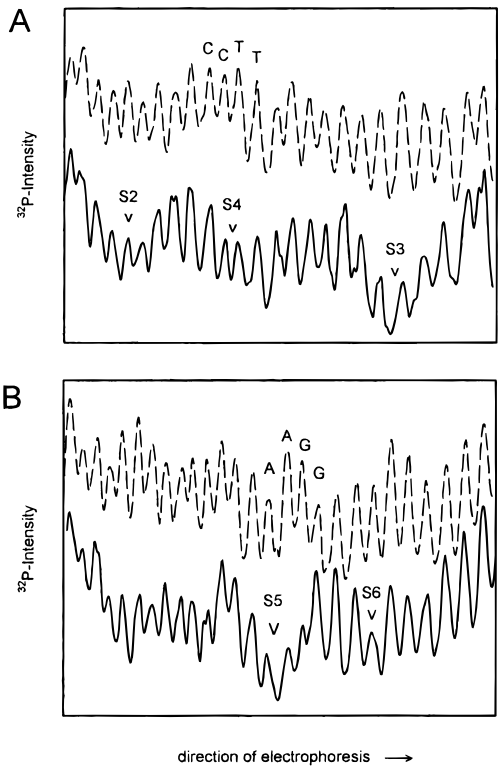

FIGURE 6: Intensity profiles for the interaction of IRF4 DBD with the λB DNA element. (A) The intensity profile for the TTCC strand of λB DNA is shown in the absence of protein (dashed line) and in the presence of IRF4 DBD (3.5 μM, solid line). The overall intensities of the lanes are normalized, the intensity plot of the control lane was moved along the abscissa to visualize both profiles more easily. The binding sites of IRF4 with the λB element are marked with S2, S3, and S4, respectively. (B) The intensity profiles obtained for the GGAA strand of λB DNA are displayed. The dashed line represents the control lane (no protein) and the binding of IRF4 DBD (7 μM) is shown in the solid line profile. The contact sites of IRF4 are indicated with S5 and S6, respectively.

are given in Table 3 (column 2). Figure 7B demonstrates the influence of the *ets* domain of PU.1 on the binding isotherms of IRF4. The dissociation constants of both contact sites, S3 and S4, decrease indicating a cooperative interaction in the ternary complex.

This apparent cooperativity should also be observed in the reverse titration experiment, i.e., the titration of PU.1 DBD to λB DNA in the presence of a saturating concentration of IRF4. The result of this footprinting experiment is shown in Figure 8A. The concentration of IRF4 used was 7 μM. At this concentration the λB site is saturated by IRF4 as can be seen from the binding isotherm shown in Figure 7B (closed symbols). The cutting pattern in the presence of only IRF4 is shown in lane 2. With increasing concentration of PU.1 DBD the presence of an additional footprint becomes evident (marked S1), this region corresponds to nucleotide positions 10−14 (Figure 1C). This contact site in the ternary complex was analyzed, and in Figure 8B the resulting binding curve (open symbols) is compared to the binding isotherm for S1 in the binary PU.1−DNA complex, already shown in Figure 3B (closed symbols). It is apparent that the binding of the *ets* domain of PU.1 to the λB site is not affected by the presence of the IRF4 DBD at saturating concentrations.

To acquire additional evidence for a cooperativity between IRF4 and PU.1, the titration experiments were repeated with a longer PU.1 construct that included the amino acids of the PEST domain. The PEST domain is apparently required for protein−protein interactions with IRF4 (*7*). The PU.1 construct we used was not phosphorylated at amino acid S148, since gel mobility shift assays have shown that the binding of the IRF4 DBD did not require phosphorylation at this position (*26*). The contacts of PU.1-PEST with the λB−DNA sequence are identical to those obtained with the PU.1 DBD (gel not shown). The resulting binding curves are shown in Figure 9B (closed symbols), and the K_d values are summarized in column 4 of Table 1. The footprinting gel demonstrating the effect of increasing IRF4 DBD concentration on the PU.1−λB complex was indistinguishable from the titration gel in Figure 7A (data not shown). The IRF4 interaction sites S3 and S4 were quantified and the binding isotherms obtained for both binding sites are shown in Figure 9A (open symbols). As found for the *ets* domain of PU.1, the binding of the IRF4 DBD to the DNA is facilitated in the presence of DNA-bound PU.1. However, contrary to the result for the PU.1 DBD, the titration of PU.1-PEST in the presence of IRF4 DBD at a saturating

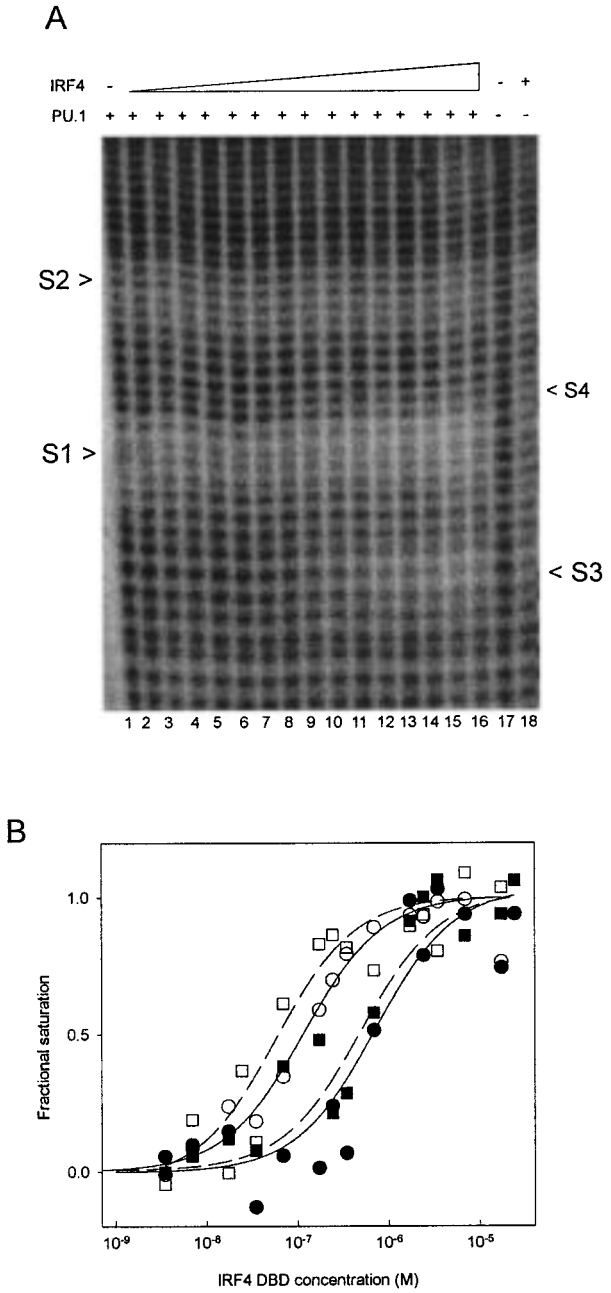

FIGURE 7: Binding of IRF4 DBD to the λB−PU.1 DBD complex. (A) IRF4 DBD is titrated with the TTCC strand of the λB−PU.1 DBD complex. 20000 cpm of ^{32}P-end-labeled DNA at ∼0.75 nM were incubated with PU.1 DBD at a final concentration of 0.1 μM prior to the addition of IRF4 DBD. Lane 1 shows the cutting pattern of PU.1 DBD at 0.1 μM. In lanes 2−16, increasing amounts of IRF4 DBD are used, the appearance of a third footprint is evident (S3). Lane 17 corresponds to the control lane (no protein), and lane 18 gives the cutting pattern with IRF4 at 3.5 μM. The protection sites of PU.1 DBD with the λB DNA are marked with S1 and S2, respectively. S3 and S4 correspond to the protected sites of IRF4 DBD. (B) The influence of DNA-bound PU.1 DBD on the binding curves for IRF4 is shown for two binding sites. The binding data indicated with closed symbols represent the binding to (●) G(17)G(18)T(19) and (■) C(8)T(9) of the λB DNA element. The corresponding binding curves in the presence of DNA-bound PU.1 DBD are shown with open symbols: (○) G(17)G(18)T(19) and (□) C(8)T(9). The data were fitted to eq 2 yielding the solid lines for S3, G(17)G(18)T(19), and the dashed lines for S4, C(8)T(9), respectively.

concentration (7 μM) revealed cooperativity (Figure 9B, open symbols). The dissociation constant of PU.1-PEST is reduced in the presence of the IRF4 DBD (column 4 of Table 1).

Table 3: Influence of DNA-Bound PU.1 on the Dissociation Constants, K_d ($\times 10^{-7}$ M), for the Interactions of IRF4 DBD with the TTCC Strand of pLBSK

nucleotide[a]	−PU.1	+PU.1 DBD	+PU.1 (106−272)
G(17)	7.60 ± 1.30[b]	1.24 ± 0.30	2.97 ± 0.60
G(18)	7.18 ± 1.08	1.05 ± 0.18	1.66 ± 0.32
T(19)	5.91 ± 0.65	1.24 ± 0.72	2.01 ± 0.44
G(17)G(18)T(19)	5.59 ± 0.60	1.17 ± 0.16	1.90 ± 0.48
C(8)T(9)	5.05 ± 1.87	0.59 ± 0.19	2.14 ± 0.86

[a] Numeration system of nucleotides is shown in Figure 1D. [b] Mean ± standard error.

To better understand how the data relate to the molecular structure of the IRF4/PU.1/λB ternary complex, we produced a model of the λB element bound to the *ets* domain of PU.1 using the atomic coordinates from the crystallographic study of PU.1 (*3*). Since the footprints of the PU.1 DBD with λB DNA element were the same as those in the crystal sequence, the three-dimensional structure was assumed to be the similar for both complexes (*20*). Figure 10 shows the resulting model of the binary PU.1−DNA complex. The positions protected from hydroxyl radical cleavage in the λB−PU.1 DBD complex are indicated with small spheres (S1, S1*, S2*). These positions map well to sites where the loops of the loop-helix-loop motif of the *ets* domain of PU.1 contact the phosphate backbone. Sites S3, S4, and S5 protected by the DNA binding domain of IRF4 in the binary IRF4−λB complex and in the ternary IRF4/PU.1/λB complex are shown as large spheres. These three IRF4 protection sites map to one face of the DNA helix downstream and roughly 90° from the PU.1 binding surface. The S4/S5 and S3 sites also straddle the edges of the major groove centered around the ISRE element (TGAA, positions 12−15, see Figure 1D). The S2 protection site shared by both proteins and the S6 site, both indicated with medium-sized spheres, is one helix turn upstream from the PU.1 recognition sequence, GGAA.

DISCUSSION

Dissociation Constants for Different PU.1−DNA Complexes. We have used two techniques to obtain equilibrium dissociation constants for different PU.1−DNA complexes. Fluorescence anisotropy measurements gave a dissociation constant (K_d) for the interaction of the *ets* domain of PU.1 with three different target sequences. With quantitative hydroxyl radical footprinting we obtained dissociation constants based on binding isotherms of particular nucleotides and of binding sites individually for both DNA strands. Within the primary S1 protection site on the TTCC strands (positions 10−14, Figure 1), no significant difference was observed between K_d derived from the binding curves of individual nucleotides and of the entire S1 protection site (see Table 1). This demonstrates that the protection of these nucleotides is part of the same molecular binding event. This is also true for the GGAA strands, for which both S1* and S2* protection sites were quantified. For a specific DNA sequence, most dissociation constants derived from binding isotherms for individual nucleotides and for the two protected sites are comparable within the error limits (see Table 2). The weaker protection of the nucleotides on the GGAA strands increases error in the analysis of those binding

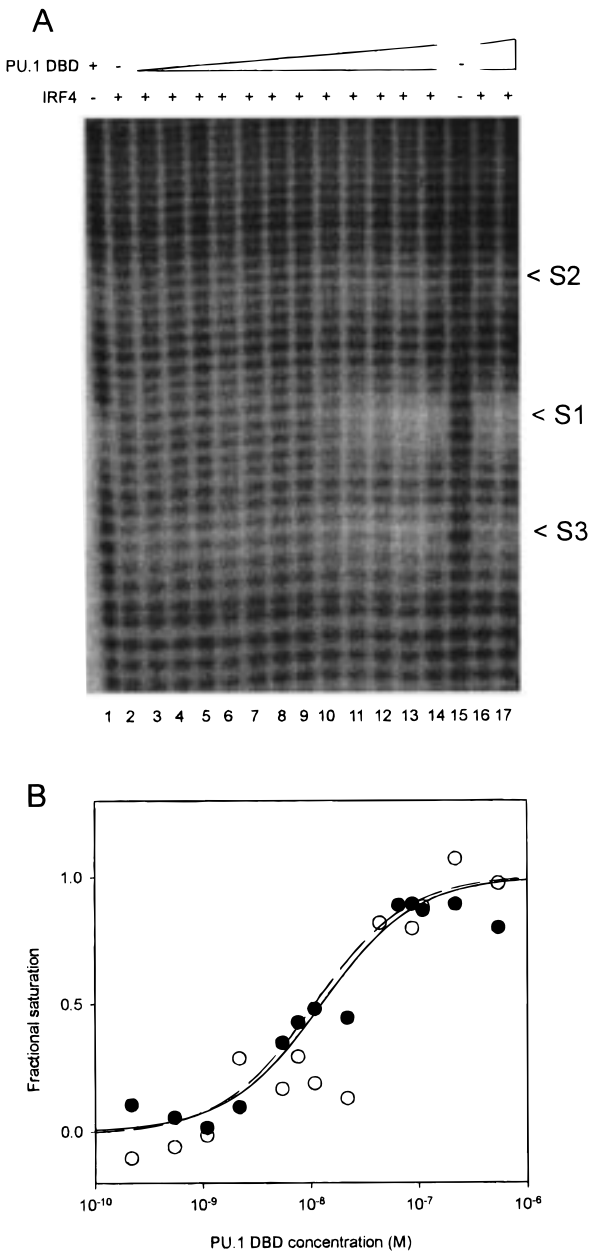

FIGURE 8: Binding of PU.1 DBD to the λB−IRF4 DBD complex. (A) The titration of PU.1 DBD to the TTCC strand of the λB−IRF4 DBD complex is followed with hydroxyl radical footprinting. 20000 cpm of ^{32}P-end-labeled DNA at ∼0.75 nM were incubated with IRF4 DBD at a final concentration of 7 μM prior to the addition of PU.1 DBD. Lane 1 gives the cutting pattern in the presence of only PU.1 DBD. Lanes 2−14, 16, and 17 demonstrate the effect of increasing amounts of PU.1 DBD to the λB−IRF4 complex and the appearance of a third footprint (S1). Lane 15 corresponds to the control lane, no protein was used. The protection sites of IRF4 are marked as S2 and S3. (B) The influence of DNA-bound IRF4 DBD on the binding curve of PU.1 DBD is displayed: data in the absence of IRF4 (●), and in the presence of the λB−IRF4 DBD complex (○). The fitted curves are shown as a solid line in the absence of IRF4, and as a dashed line in the presence of IRF4, respectively.

isotherms and is most likely the reason for the discrepancy of K_d values within one DNA fragment.

A comparison of the binding affinities determined by footprinting for the three different DNA sequences indicates that the *ets* domain of PU.1 binds most strongly to the TTCC strand of the λB site (pLBSK) (Table 1). The binding

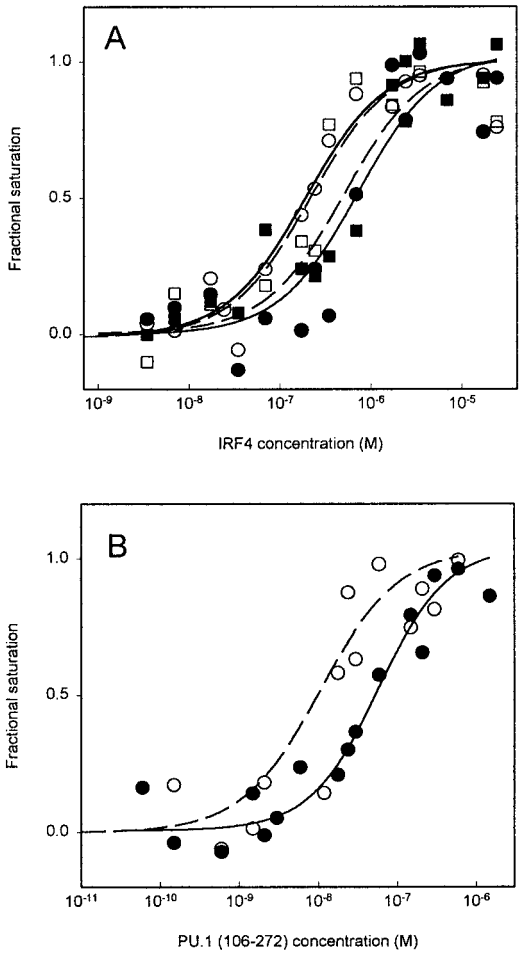

FIGURE 9: Interactions of IRF4 DBD and PU.1-PEST with the λB site. (A) The influence of DNA-bound PU.1-PEST on the binding of IRF4 DBD is shown. The binding data indicated with closed symbols represent the binding of (●) G(17)G(18)T(19) and (■) C(8)T(9) to the λB DNA element. The corresponding binding curves in the presence of PU.1 (106−272) at 0.3 μM are shown with open symbols: (○) G(17)G(18)T(19) and (□) C(8)T(9). The data were fitted to eq 2 and yielded the solid lines for S3, G(17)G(18)T(19), and the dashed lines for S4, C(8)T(9), respectively. (B) The influence of DNA-bound IRF4 DBD on the binding of PU.1-PEST is demonstrated: data in the absence of IRF4 (●), and in the presence of IRF4 DBD at 7 μM (○). The resulting fitted curves are shown as a solid line (without IRF4) and as a dashed line (with IRF4).

affinity of the PU.1-PEST construct (amino acids 106−272) to the TTCC strand of λB DNA was lower than that for the PU.1 DBD construct (column 4 of Table 1) possibly due to the net negative change of the PEST domain.

For the different GGAA strands we observed a lower K_d for the interactions in the PU.1−pPUSK complex, whereas the binding affinities of PU.1 DBD for pCRYSK and pLBSK were similar (compare columns 1 and 3 with column 2 of Table 2).

The dissociation constants for the PU.1−DNA complexes that we obtained with fluorescence polarization measurements are approximately 1 order of magnitude higher than those determined by footprinting (Figure 5 and Table 2). We attribute this discrepancy to the different length of the DNA fragments used in both techniques and variations in the buffer conditions used in the two experiments. The DNA fragments used in the fluorescence measurements were 20-bp long and started with nucleotide position 0 (Figure 1) immediately

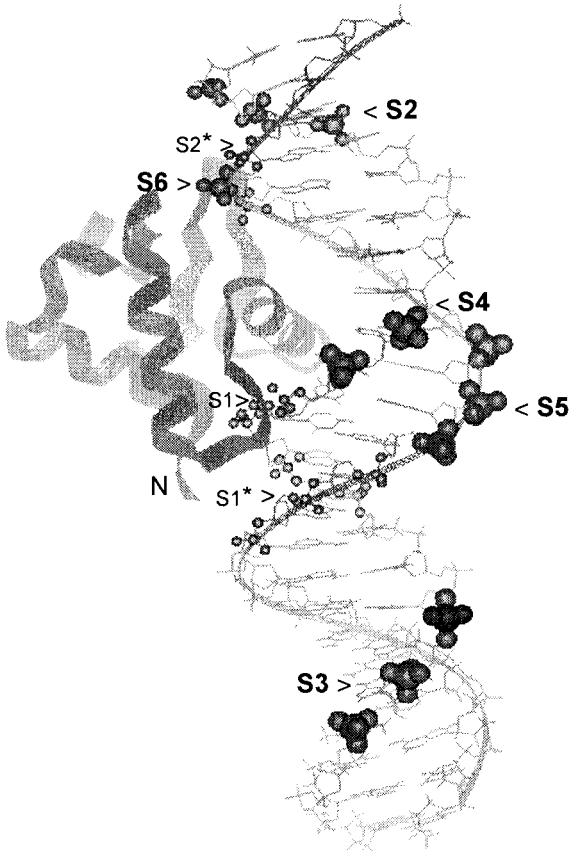

FIGURE 10: Model of the λB−PU.1 DBD complex showing the sites protected from hydroxyl radical cleavage in the ternary PU.1/IRF4/λB complex. The atomic coordinates from the PU.1−DNA crystal structure were used to display the PU.1−DNA complex with its induced 8° bent in the DNA (*3*, PDB accession code: 1PUE). The DNA in the crystal structure was extended by adding on 5 base pairs of the appropriate sequence modeled as a *B*-form duplex DNA with a helical repeat of 10.5 bp/turn using Insight II (Molecular Simulation Inc., San Diego, CA). The phosphate groups at positions protected by PU.1 DBD are shown as small spheres and labeled with S1, S2, S1*, and S2* as in Figure 1. The phosphate groups of the major contact sites of IRF4 DBD are indicated as large spheres and marked as S3, S4, and S5 (large bold print) corresponding to Figures 1D, 6A, and 6B. The S2 and S6 sites which are weakly protected are illustrated with medium size spheres. PU.1 is represented as a backbone ribbon trace with the N-terminus (N) close to the S1 and S1* protection sites.

adjacent to the protected site S2. Fraying of the DNA ends could result in a weaker interaction between PU.1 and the S2 site on the short DNA fragments relative to the respective contact with the longer DNA fragments.

Interactions of IRF4 with DNA. The dissociation constant for the interaction of IRF4 DBD with λB site determined here is approximately five times lower than the K_d values of the PU.1 DBD and PU.1-PEST. Our hydroxyl radical footprinting results are consistent with methylation protection data which showed that all guanines in the S3 and S5 protection sites were protected from methylation (*4, 11*).

Interactions of IRF4 and PU.1 in the PU.1/IRF4/λB DNA Complex. We determined the interactions of the DNA binding domains of PU.1 and IRF4 in their ternary complex with the λB DNA element. As demonstrated in Figure 7A, the contact sites in the ternary complex are the sum of the contact sites that are observed in the respective binary protein−DNA complexes. Importantly, the resulting footprint is identical, regardless of the order in which the two proteins were added to the DNA (lanes 15 in Figures 7A and 8A).

The binding affinity of IRF4 DBD for the DNA is increased about 5-fold by the presence of the PU.1 DBD (Figure 7B); however, the binding of the PU.1 DBD is not affected by the presence of the IRF4−DNA complex (Figure 8B). This is not compatible with a mutually cooperative interaction between the DNA binding domains of PU.1 and IRF4 which should be independent of the explicit order in which the ternary complex was formed. Quantitative evidence for cooperativity was found in titrations employing the longer PU.1-PEST construct in the presence of IRF4−λB (Figure 9B).

Refinement of the Model for the IRF4 Interaction with PU.1. The model illustrated in Figure 10 indicates that the IRF4 DBD binds to the helix surface defined by the protection sites S3, S4, and S5. The similarity of the K_d values for the interaction of IRF4 DBD with S3 and S4 (Table 3) indicates that the protection of both sites is part of the same molecular binding event. In the ternary PU.1/IRF4/λB complex, the PU.1 DBD lies in the adjacent major groove on the opposite side of the DNA helix. The centers of the protected surfaces in the PU.1 DBD site and those in the IRF4 binding site are offset by about 90°. The proximity of the DNA binding domains of PU.1 and IRF4 in the ternary complex supports the possibility of protein−protein interactions between both domains as proposed previously (*13*). Our model also agrees with the cooperative interactions we observed between the longer PU.1 construct containing the PEST domain and the DNA-bound IRF4 DBD. In PU.1, the PEST domain is located N-terminal to the DNA binding domain ("N" in Figure 10) and even closer to the presumed binding site of IRF4 than the *ets* domain of PU.1. Protein−protein interactions between the PEST domain of PU.1 and the IRF4 DBD are therefore probably the source of additional binding energy that yield the observed cooperativity.

The model in Figure 10 also shows the position of contact site S2, shared by both DNA binding domains, and another protected site, S6. Since S6 on the GGAA strand is close to S2 on the TTCC strand it can be considered part of the S2 protection site and will be discussed together with S2. The protection of S2 by PU.1 in the binary and ternary complexes arises from the proximity of the second loop of the loop-helix-loop binding surface. However, the distance of S2 from the presumed binding site of IRF4 DBD (between S4/S5 and S3) appears to rule out the possibility that S2 protection in the binary IRF4−λB complex originates from the same binding event that leads to protection at the S3, S4, and S5 sites. Note that the protection of S2 by IRF4 DBD was markedly weaker than the protection observed for the other IRF4 sites (S3−S5). Also, an equally weak protection of the corresponding nucleotides was observed in the three different binary PU.1 DBD−DNA complexes (Figure 1). This raises the possibility that the weak protection of the nucleotides within S2 originates from a structural change in the DNA rather than from protein contacts. However, according to the PU.1−DNA crystal structure, the DNA helix in vicinity of S2 is not visibly altered compared to other regions of the complex (Figure 10) although a small structural distortion of the DNA helix resulting in weak protection of the phosphate backbone cannot be ruled out.

The model we present for the interactions between subdomains of IRF4 and PU.1 and the λB element provides detailed information about the spatial relation of both DNA binding domains in the ternary complex. It should be noted, that previously described cooperative interactions between the full length PU.1 and IRF4 involved the phosphorylated PEST domain and the C-terminal domain of IRF4 (*13*). The model presented in Figure 10 is entirely consistent with increased protein−protein interactions between the full-length proteins which would likely result in greater cooperativity. The extension of quantitative investigations such as those presented here to longer protein constructs and to the full-length proteins will help identify the relative contributions of individual domains of each protein in the cooperative interactions that take place between the two proteins in vivo. Such studies will also aid in the quantitative analysis of the role of phosphorylation in cooperativity and in the transcriptional function of the PU.1/IRF4/λB DNA complex.

REFERENCES

1. Wasylyk, B., Hahn, S. L., Giovane, A. (1993) *Eur. J. Biochem. 211*, 7−18.
2. Nye, J. A., Petersen, J. M., Gunther, C. V., Jonsen. M. D., and Graves, B. J. (1992) *Genes Dev. 6*, 975−990.
3. Kodandapani, R., Pio, F., Ni, C.-Z., Piccialli, G., Klemsz, M., McKercher, S., Maki, R. A., and Ely, K. R. (1996) *Nature 380*, 456−460.
4. Eisenbeis, C. F., Singh, H., and Storb, U. (1995) *Genes Dev. 9*, 1377−1387.
5. Au, W. C., Moore, P. A., Lowther, W., Juang, Y. T., and Pitha, P. M. (1995) *Proc. Natl. Acad. Sci U.S.A. 92*, 11657−11661.
6. Matsuyama, T., Grossman, S., Mittrucker, H.-W., Siderovski, D., Kiefer, F., Kawakami, T., Richardson, C. D., Taniguchi, T., Yoshigana, S., and Mak, T. (1995) *Nucleic Acids Res. 23*, 2127−2136.
7. Pongubala, J. M. R., Nagulapalli, S., Klemsz, M., McKercher, S. R., Maki, R. A., and Atchinson, M. L. (1992) *Mol. Cell. Biol. 12*, 368−378.
8. Yamagata, T., Nishida, J., Tanaka, T., Sakai, R., Mitani, K., Yoshida, M., Taniguchi, T., Yazaki, Y., and Hirai, H. (1996) *Mol. Cell. Biol. 16*, 1283−1294.
9. Taniguchi, T., Harada, H., and Laphier, M. (1995) *J. Canc. Res. Clin. Oncol. 121*, 516−520.
10. Judde, J., and Max, E. (1992) *Mol. Cell. Biol. 12*, 5206−5216.
11. Eisenbeis, C. F., Singh, H., and Storb, U. (1993) *Mol. Cell. Biol. 13*, 6452−6464.
12. Pongubala, J. M. R., Van Beveren, C., Nagulapalli, S., Klemsz, M. J., McKercher, S. R., Maki, R. A., and Atchison, M. L. (1993) *Science 259*, 1623−1625.
13. Brass, A. L., Kehrli, E., Eisenbeis, C. F., Storb, U., and Singh, H. (1996) *Genes Dev. 10*, 2335−2347.
14. Tullius, T. D., and Dombroski, B. A. (1986) *Proc. Natl. Acad. Sci. U.S.A. 83*, 5469−5473.
15. Petri, V., and Brenowitz, M. (1997) *Curr. Opin. Biotechnol 8*, 36−44.
16. King, P. A., Jamison, E., Strahs, D., Anderson, V. E., and Brenowitz, M. (1993) *Nucleic Acids Res. 21*, 2473−2478.
17. Strahs, D., and Brenowitz, M. (1994) *J. Mol. Biol. 294*, 494−510.
18. Sclavi, B., Woodson, S., Sullivan, M., Chance, M. R., and Brenowitz, M. (1997) *J. Mol. Biol. 297*, 144−159.
19. Shadle, S. E., Allen, D. F., Guo, H., Pogozelski, W. K., Bashkin, J. S., and Tullius, T. D. (1997) *Nucleic Acids Res. 25*, 850−860.
20. Gross, P., Arrowsmith, C. H., and Macgregor, R. B., Jr. (1998) *Biochemistry 37*, 5129−5135.
21. Cheng, X., Morin, P. E., Harms, A. C., Bruce, J. E., Ben-David, Y., and Smith R. D. (1996) *Anal. Biochem. 239*, 35−40.
22. Brenowitz, M., Senear, D. F., Shea, M. A., and Ackers, G. K. (1986) *Methods Enzymol. 130*, 132−181.
23. Brenowitz, M., and Senear, D. F. (1989) *In Current Protocols in Molecular Biology* (Ausubel, F. M., Brent, R., Kingston, R. E., Moore, D. D., Seidman, J. G., Smith, J. A., and Struhl, K. Eds.) John Wiley and Sons, New York.
24. Brenowitz, M., Senear, D., Jamison, E., and Dalma-Weiszhaus, D. (1993) *in Footprinting of Nucleic Acid−Protein Complexes* (Revzin, A. Ed.) 1−44, Academic Press, San Diego.
25. Lundblad, J. R., Laurance, M., and Goodman, R. H. (1996) *Mol. Endocrinol. 10*, 607−612.
26. Yee, A. A., Yin, P., Siderovski, D. P., Mak, T. W., Litchfield, D. W., and Arrowsmith, C. H. (1998) *J. Mol. Biol*. (in press).

BI9731448